

PREPARED FOR SUBMISSION TO JHEP

FEBRUARY 23, 2022

Complete NLO corrections to W^+W^+ scattering and its irreducible background at the LHC

Benedikt Biedermann, Ansgar Denner, Mathieu Pellen

Universität Würzburg, Institut für Theoretische Physik und Astrophysik, Emil-Hilb-Weg 22, 97074 Würzburg, Germany

E-mail: benedikt.biedermann@physik.uni-wuerzburg.de,
ansgar.denner@physik.uni-wuerzburg.de,
mathieu.pellen@physik.uni-wuerzburg.de

ABSTRACT: The process $pp \rightarrow \mu^+\nu_\mu e^+\nu_e jj$ receives several contributions of different orders in the strong and electroweak coupling constants. Using appropriate event selections, this process is dominated by vector-boson scattering (VBS) and has recently been measured at the LHC. It is thus of prime importance to estimate precisely each contribution. In this article we compute for the first time the full NLO QCD and electroweak corrections to VBS and its irreducible background processes with realistic experimental cuts. We do not rely on approximations but use complete amplitudes involving two different orders at tree level and three different orders at one-loop level. Since we take into account all interferences, at NLO level the corrections to the VBS process and to the QCD-induced irreducible background process contribute at the same orders. Hence the two processes cannot be unambiguously distinguished, and all contributions to the $\mu^+\nu_\mu e^+\nu_e jj$ final state should be preferably measured together.

Contents

1	Introduction	2
2	Details of the calculation	3
2.1	Real corrections	6
2.2	Virtual corrections	6
2.3	Validation	8
3	Numerical Results	8
3.1	Input parameters and selection cuts	8
3.2	Integrated cross section	10
3.3	Differential distributions	13
4	Conclusions	18

1 Introduction

With the discovery of the Higgs boson in 2012 at the Large Hadron Collider (LHC), a new era in particle physics has started. On the one hand, this discovery substantiated the last missing ingredient of the meanwhile well-established Standard Model of elementary particles. On the other hand, it represents the dawn of a new paradigm of precision physics aiming at the investigation of electroweak (EW) symmetry breaking. Thereby, vector-boson scattering (VBS) plays a fundamental role owing to its sensitivity to the quartic non-Abelian gauge couplings and to the Higgs sector of the Standard Model as a whole.

At a hadron collider, the scattering of massive vector bosons occurs if partons in the two incoming protons radiate W or Z bosons that scatter off each other. The leptonic decay products of the scattered bosons in association with two jets radiated from the incoming partons in forward direction give rise to a typical signature that can be enhanced over the irreducible background with dedicated VBS event selections. Among the various leptonic final states, the channel with two equally charged leptons and two neutrinos, the so-called same-sign WW channel, has been identified as the most promising candidate for discovery [1, 2]. Owing to the limited number of partonic channels that allow for such a leptonic final state, the irreducible QCD background is smaller than in the other VBS channels.

During run I at the LHC, evidence for VBS in the same-sign WW channel has been reported by both the ATLAS [3, 4] and CMS [5] collaborations. Recently the CMS collaboration has observed this process at the LHC with data from run II [6]. It is therefore essential to have precise and appropriate predictions for both the VBS process as well as for its irreducible background. In this context, *precise* means next-to-leading order (NLO) QCD and EW accuracy, and *appropriate* characterises predictions that are directly comparable with experimental measurements.

In this article, we present the first complete computation of all NLO QCD and EW corrections to the process $pp \rightarrow \mu^+ \nu_\mu e^+ \nu_e jj$. At leading order (LO), the cross section receives contributions of three different orders in the EW and strong coupling constants α and α_s : 1) a purely EW contribution at $\mathcal{O}(\alpha^6)$ that includes among others the actual VBS mechanism, 2) a QCD-induced contribution at $\mathcal{O}(\alpha_s^2 \alpha^4)$, and 3) an interference contribution at $\mathcal{O}(\alpha_s \alpha^5)$. While the purely EW contribution contains, besides the VBS contribution, also irreducible background contributions and triple W-boson production, we will nevertheless sometimes refer to the EW production mode as VBS process in the following. From a theoretical point of view, the three LO contributions can be separated in a gauge-invariant way based on the different orders in the coupling constants. From an experimental point of view, dedicated phase-space cuts, including tagging jets with large rapidity separation and invariant mass, have been designed to enhance the actual VBS contribution from its QCD-induced and EW-induced irreducible background.

Consequently, the complete NLO contribution involves the four different orders $\mathcal{O}(\alpha^7)$, $\mathcal{O}(\alpha_s \alpha^6)$, $\mathcal{O}(\alpha_s^2 \alpha^5)$, and $\mathcal{O}(\alpha_s^3 \alpha^4)$. Since some of these single NLO contributions furnish corrections to more than one LO contribution, it is not possible to unambiguously attribute a

given type of correction to a given underlying Born process. Hence, at NLO one cannot distinguish the different production mechanisms, in particular EW- and QCD-induced production modes, as they are naturally mutually contaminated.

Parts of the NLO corrections to the process $pp \rightarrow \mu^+ \nu_\mu e^+ \nu_e jj$ have already been computed in the literature. These calculations focused on NLO QCD corrections for both the VBS process [7–10] and its QCD-induced irreducible background process [10–14]. We have already reported in Ref. [15] on the surprisingly large NLO EW corrections to the VBS process. The aim of the present article is to provide the complete NLO corrections to the $\mu^+ \nu_\mu e^+ \nu_e jj$ final state, based on the complete LO and NLO matrix elements and including all interference contributions and all off-shell effects.

This article is organised as follows. In Sect. 2, details of the calculation are described. In particular, the different types of real and virtual corrections, and the validation of our results are reviewed. In Sect. 3, numerical results are presented for integrated cross sections and differential distributions. The article concludes with a summary and final remarks in Sect. 4.

2 Details of the calculation

The hadronic process studied is defined at LO as

$$pp \rightarrow \mu^+ \nu_\mu e^+ \nu_e jj. \quad (2.1)$$

Owing to charge conservation, there are no gluon-induced or photon-induced contributions at LO. Furthermore, bottom quarks in the initial state do not contribute as these would lead to a final state with massive top quarks which falls under a different experimental signature. At the amplitude level, the process receives two different types of contributions: a pure EW part at the order $\mathcal{O}(g^6)$ (which we call sometimes simply VBS contribution) and a QCD-induced part at the order $\mathcal{O}(g_s^2 g^4)$ with g and g_s being the EW and QCD coupling constants, respectively. Figure 1 shows sample tree-level diagrams for the partonic sub-process $u\bar{d} \rightarrow \mu^+ \nu_\mu e^+ \nu_e u\bar{d}$. The top row of diagrams illustrates the actual VBS process at $\mathcal{O}(g^6)$ with its characteristic VBS topology of two W bosons with space-like momenta that scatter into two W bosons with time-like momenta. These contributions are referred to as t -channel diagrams since the two incoming quark/anti-quark lines are connected to outgoing quark/anti-quark lines. For identical outgoing quarks or anti-quarks also u -channel diagrams are obtained by exchanging the two outgoing quarks or anti-quarks. The s -channel diagram on the left in the bottom row of order $\mathcal{O}(g^6)$ contributes to the irreducible EW background. In general, s -channel diagrams are diagrams where the incoming quark and anti-quark are connected via fermion lines. There are also s -channel diagrams contributing to triple gauge-boson production ($W^+ W^+ W^-$) (bottom middle). Finally, the diagram on the bottom right is an example of a QCD-induced contribution at order $\mathcal{O}(g_s^2 g^4)$. This contribution exclusively consists of diagrams where a gluon is connecting the two quark lines and thus, by construction, cannot involve VBS topologies. Thus, at the level of squared amplitudes, three gauge-invariant contributions exist: the pure EW contribution of order $\mathcal{O}(\alpha^6)$, the QCD-induced contribution

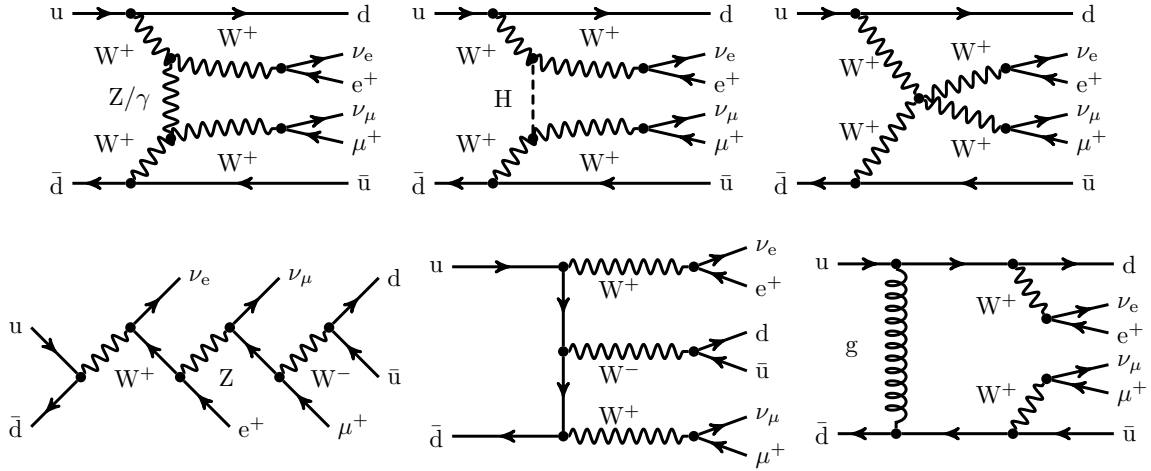


Figure 1: Sample tree-level diagrams that contribute to the process $pp \rightarrow \mu^+ \nu_\mu e^+ \nu_e jj$.

of order $\mathcal{O}(\alpha_s^2 \alpha^4)$, and interferences of the order $\mathcal{O}(\alpha_s \alpha^5)$. Owing to the colour structure, these interferences occur only if diagrams of different quark flow between initial and final state are multiplied with each other. Thus, order- $\mathcal{O}(\alpha_s \alpha^5)$ contributions appear only in partonic channels that involve contributions of two different kinematic channels (s , t , u). For example, in Fig. 1, the contraction of the QCD-induced diagram (bottom right) with the VBS diagrams (top row) necessarily vanishes due to colour structure, while the corresponding contraction with the EW s -channel background diagrams (bottom left and bottom middle) leads to a non-zero interference contribution at order $\mathcal{O}(\alpha_s \alpha^5)$. We stress that we include in our calculation all possible contributions at the orders $\mathcal{O}(\alpha^6)$, $\mathcal{O}(\alpha_s \alpha^5)$, and $\mathcal{O}(\alpha_s^2 \alpha^4)$ that belong to the hadronic process in Eq. (2.1). A list of all contributing independent partonic channels is given in Table 1, which provides also information on contributing kinematic channels and interferences.

At NLO, we compute both the QCD and EW corrections to each LO contribution. This leads to four possible NLO orders: $\mathcal{O}(\alpha^7)$, $\mathcal{O}(\alpha_s \alpha^6)$, $\mathcal{O}(\alpha_s^2 \alpha^5)$, and $\mathcal{O}(\alpha_s^3 \alpha^4)$. The situation is represented graphically in Fig. 2.¹ The order $\mathcal{O}(\alpha^7)$ contributions are simply the NLO EW corrections to the EW-induced LO processes. They have already been presented in Ref. [15] for a fixed scale. Similarly, the order $\mathcal{O}(\alpha_s^3 \alpha^4)$ contributions furnish the QCD corrections to the QCD-induced process, which have been computed in Refs. [11, 13, 17].

For the orders $\mathcal{O}(\alpha_s \alpha^6)$ and $\mathcal{O}(\alpha_s^2 \alpha^5)$, a simple separation of the EW-induced process and the QCD-induced process is not possible any more, also for the dominant uu partonic channel. Indeed, the order $\mathcal{O}(\alpha_s \alpha^6)$ contains QCD corrections to the VBS process as well as EW corrections to the LO interference. The QCD corrections have already been computed in the VBS approximation in Refs. [7–9, 13, 14]. This means that the s -channel diagrams as

¹Such a classification in powers of α_s and α can also be found in Ref. [16].

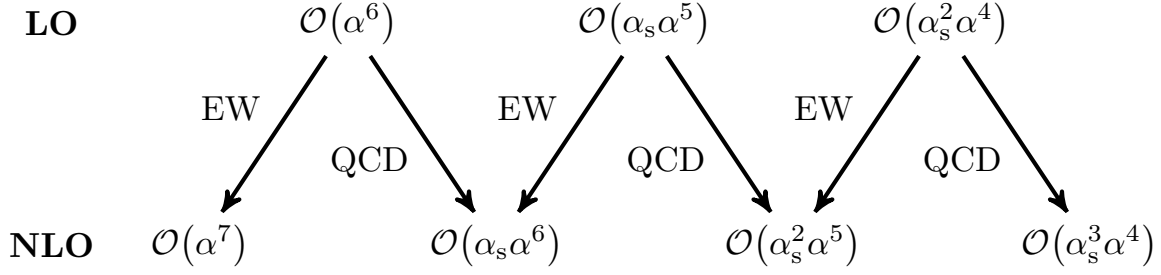


Figure 2: All contributing orders at both LO and NLO for the process $pp \rightarrow \mu^+ \nu_\mu e^+ \nu_e jj$.

well as the interference of t - and u -channel diagrams are neglected. In this approximation, the interferences of the LO VBS and QCD-induced contribution are vanishing. Similarly, the order $\mathcal{O}(\alpha_s^2 \alpha^5)$ contains EW corrections to the QCD-induced contribution as well as QCD corrections to the LO interference. These corrections have never been computed previously and are presented here for the first time.

All the tree-level and one-loop matrix elements have been obtained from the computer code RECOLA [18, 19] based on the COLLIER [20, 21] library. Throughout, the complex-mass scheme [22, 23] is used. All results have been obtained in two independent Monte Carlo programs that have already been used for the computations of NLO QCD and EW

partonic channel	interferences at $\mathcal{O}(\alpha_s \alpha^5)$	kinematic channels
$uu \rightarrow \mu^+ \nu_\mu e^+ \nu_e dd$	yes	t, u
$uc/cu \rightarrow \mu^+ \nu_\mu e^+ \nu_e ds$	no	t
$cc \rightarrow \mu^+ \nu_\mu e^+ \nu_e ss$	yes	t, u
$u\bar{d}/\bar{d}u \rightarrow \mu^+ \nu_\mu e^+ \nu_e d\bar{u}$	yes	t, s
$u\bar{d}/\bar{d}u \rightarrow \mu^+ \nu_\mu e^+ \nu_e s\bar{c}$	no	s
$u\bar{s}/\bar{s}u \rightarrow \mu^+ \nu_\mu e^+ \nu_e d\bar{c}$	no	t
$c\bar{d}/\bar{d}c \rightarrow \mu^+ \nu_\mu e^+ \nu_e s\bar{u}$	no	t
$c\bar{s}/\bar{s}c \rightarrow \mu^+ \nu_\mu e^+ \nu_e d\bar{u}$	no	s
$c\bar{s}/\bar{s}c \rightarrow \mu^+ \nu_\mu e^+ \nu_e s\bar{c}$	yes	t, s
$\bar{d}\bar{d} \rightarrow \mu^+ \nu_\mu e^+ \nu_e \bar{u}\bar{u}$	yes	t, u
$\bar{d}\bar{s}/\bar{s}\bar{d} \rightarrow \mu^+ \nu_\mu e^+ \nu_e \bar{u}\bar{c}$	no	t
$\bar{s}\bar{s} \rightarrow \mu^+ \nu_\mu e^+ \nu_e \bar{c}\bar{c}$	yes	t, u

Table 1: Leading-order partonic channels contributing to the hadronic process $pp \rightarrow \mu^+ \nu_\mu e^+ \nu_e jj$. The middle column indicates whether the channel gives rise to an interference contribution at $\mathcal{O}(\alpha_s \alpha^5)$ or not. The right column specifies the contributing kinematic channels.

corrections for high-multiplicity processes described in Refs. [15, 24–26] and Refs. [15, 27–29], respectively.

2.1 Real corrections

In this section, the real NLO corrections (both of QCD and QED origin) to all LO contributions are discussed. To handle the associated IR divergences, the dipole-subtraction method for QCD [30] and its extension to QED [31] have been employed. The colour-correlated matrix elements needed for the subtraction procedure are obtained directly from RECOLA.

At the order $\mathcal{O}(\alpha^7)$, the real corrections consist simply of all photon radiations off any charged particle, *i.e.* all contributions of the type $pp \rightarrow \mu^+ \nu_\mu e^+ \nu_e jj \gamma$ originating from the LO EW production mode. At the order $\mathcal{O}(\alpha_s \alpha^6)$, there are two types of real radiation. First, there is the QCD radiation $pp \rightarrow \mu^+ \nu_\mu e^+ \nu_e jjj$ with underlying EW Born. Second, there is photon radiation $pp \rightarrow \mu^+ \nu_\mu e^+ \nu_e jj \gamma$ from the LO interferences. While both types of real radiation contribute at order $\mathcal{O}(\alpha_s \alpha^6)$, each type requires a different subtraction procedure. In the same way, the order $\mathcal{O}(\alpha_s^2 \alpha^5)$ features two types of real contributions. First, photon radiation from the QCD-induced process and, second, QCD radiation from the LO interference contributions. Finally, the QCD radiation to the QCD-induced process of the type $pp \rightarrow \mu^+ \nu_\mu e^+ \nu_e jjj$ contributes at the order $\mathcal{O}(\alpha_s^3 \alpha^4)$.

Note that the QCD radiation of type $pp \rightarrow \mu^+ \nu_\mu e^+ \nu_e jjj$ includes both gluon radiation from any coloured particle as well as quark/anti-quark radiation from $g\bar{q}$ and gq initial states. The corresponding partonic channels can systematically be obtained from the list of partonic channels at LO given in Table 1 by first attaching an additional gluon to the final state, and then crossing this gluon with one of the quarks or anti-quarks in the initial state. In the same way, real radiation from photon-induced contributions of the type $\gamma q/\gamma \bar{q} \rightarrow \mu^+ \nu_\mu e^+ \nu_e jjj$ contributes at the orders $\mathcal{O}(\alpha^7)$, $\mathcal{O}(\alpha_s \alpha^6)$, and $\mathcal{O}(\alpha_s^2 \alpha^5)$. We have computed these contributions separately (*c.f.* Table 4) but do not include them in our default NLO corrections.

2.2 Virtual corrections

In the same way as for the real corrections, the various virtual corrections contributing at each order are described in the following. All the virtual corrections have been obtained from RECOLA in association with the COLLIER library which is used to calculate the one-loop scalar [32–35] and tensor integrals [36–38] numerically. Some of the virtual diagrams computed are represented in Fig. 3. On the left-hand side, an EW correction to the EW amplitude, a diagram of order $\mathcal{O}(g^8)$ featuring an 8-point function, is shown. The diagram of order $\mathcal{O}(g_s^2 g^6)$ in the middle can either be interpreted as an EW correction to the QCD-induced process or as a QCD correction to the EW-induced process and illustrates that both processes cannot be separated any more once the full NLO corrections are included. Finally, on the right hand-side a QCD loop correction to the QCD-induced amplitude is displayed.

In order to understand the emergence of different orders in the EW and QCD coupling at the level of the virtual corrections, one starts again at amplitude level and considers all possible interferences of the Born contributions at order $\mathcal{O}(g^6)$ and $\mathcal{O}(g_s^2 g^4)$ with the virtual amplitudes

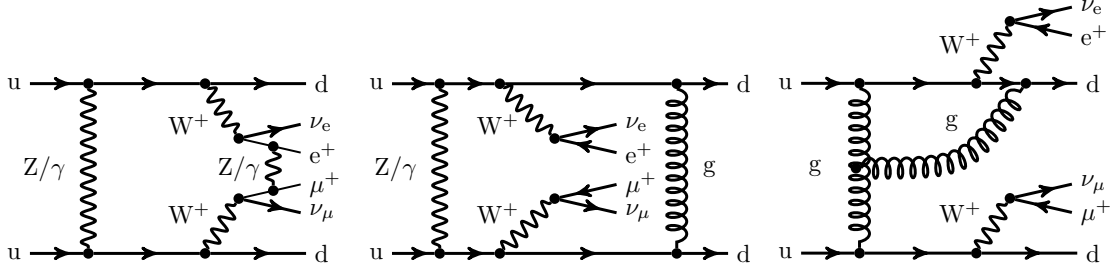


Figure 3: Sample one-loop level diagrams contributing to the process $pp \rightarrow \mu^+ \nu_\mu e^+ \nu_e jj$.

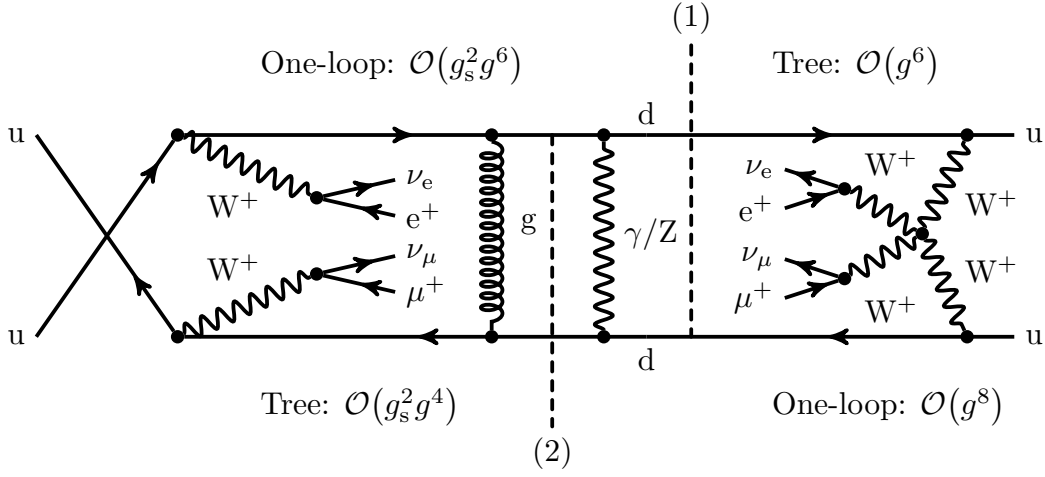


Figure 4: Contribution to the squared matrix element at the order $\mathcal{O}(\alpha_s \alpha^6)$. It can be viewed as an amplitude of order $\mathcal{O}(g_s^2 g^6)$ interfered with the LO EW amplitude [cut (1)]. On the other hand, it can be seen as an EW correction to the EW amplitude interfered with the LO QCD amplitude [cut (2)]. Owing to the colour structure, the illustrated contractions necessarily connect t - and u -channel contributions.

at the orders $\mathcal{O}(g^8)$, $\mathcal{O}(g_s^2 g^6)$, and $\mathcal{O}(g_s^4 g^4)$. At the order $\mathcal{O}(\alpha^7)$, the virtual corrections consist simply of EW corrections to the EW tree-level amplitude interfered with the EW tree-level amplitude. Concerning the order $\mathcal{O}(\alpha_s \alpha^6)$, there are different types of contributions. One first considers the insertions of gluons into the purely EW tree-level amplitude as well as the EW corrections to the QCD-induced tree-level amplitude leading to a one-loop amplitude at $\mathcal{O}(g_s^2 g^6)$ (see middle diagram of Fig. 3 for a diagrammatic example). This one-loop amplitude is then interfered with the EW tree-level amplitude at $\mathcal{O}(g^6)$. The contraction is illustrated at the level of squared amplitudes in Fig. 4 via the cut along the dashed line number (1). Second, the EW corrections to the EW tree-level amplitude at $\mathcal{O}(g^8)$ contracted with the QCD-induced LO amplitude at $\mathcal{O}(g_s^2 g^4)$ lead to yet another contribution of order $\mathcal{O}(\alpha_s \alpha^6)$.

This corresponds to the cut along the dashed line number (2) in Fig. 4. While real photon radiation and real QCD radiation are still distinguishable at the level of squared amplitudes, Fig. 4 illustrates that this is not the case any more for the virtual corrections. The situation is similar at the order $\mathcal{O}(\alpha_s^2\alpha^5)$. First, there are interferences of the QCD-induced tree-level amplitude with QCD corrections to the EW-induced LO amplitude and the EW corrections to the QCD-induced LO amplitude. Second, the gluon insertions in the QCD-induced tree-level amplitude, interfered with the EW-induced tree-level amplitude lead to another contribution at order $\mathcal{O}(\alpha_s^2\alpha^5)$. Finally, the virtual contributions of order $\mathcal{O}(\alpha_s^3\alpha^4)$ consist simply of the QCD corrections to the QCD-induced tree-level amplitude contracted with the QCD-induced tree-level amplitude.

2.3 Validation

The computation has been done with two different Monte Carlo programs providing thus an independent check of the phase-space integration and the treatment of IR singularities. These two Monte Carlo programs have already shown to be reliable when computing both NLO QCD and EW corrections for a variety of processes [15, 24–29]. The photon-induced contributions have been implemented in one of these Monte Carlo codes, but have been cross-checked with independent programs for vector-boson pair production [25, 26]. While all amplitudes are obtained from RECOLA, the computation has been performed with two different libraries of the COLLIER [20, 21] program, apart from the purely EW virtual amplitudes. The results obtained at the integration level are in excellent numerical agreement demonstrating thus the stability of the virtual contribution. The virtual corrections of order $\mathcal{O}(\alpha_s^3\alpha^4)$ for the uu channel obtained from RECOLA agree within at least 6 digits with the ones obtained with MADLOOP [39], part of the MADGRAPH5_AMC@NLO [16] framework for more than 99% of 3000 phase-space points generated randomly. Finally, we recall that the NLO computation at the order $\mathcal{O}(\alpha^7)$ reported in Ref. [15] (computed with fixed scale) has already undergone several validations. These comprise a phase-space point comparison of representative tree-level matrix elements squared and a comparison for the dominant channels against an NLO double-pole approximation. The implementation of the double-pole approximation has been automatised and used in Refs. [28, 29].

3 Numerical Results

3.1 Input parameters and selection cuts

The results presented are for the LHC operating at a centre-of-mass energy of 13 TeV. As parton distribution functions (PDF) we use the NLO NNPDF-3.0 QED set with $\alpha_s(M_Z) = 0.118$ [40, 41], interfaced to our Monte Carlo programs via LHAPDF 6.1.5 [42, 43]. We have employed the fixed $N_F = 5$ flavour scheme throughout. The EW collinear initial-state splittings are handled within the DIS factorisation scheme [44, 45], while the QCD ones are

treated by $\overline{\text{MS}}$ redefinition of the PDF. We use the same PDF for LO and NLO predictions. The renormalisation and factorisation scales are set dynamically as

$$\mu_{\text{ren}} = \mu_{\text{fac}} = \sqrt{p_{\text{T},j1} p_{\text{T},j2}}, \quad (3.1)$$

where $p_{\text{T},ji}$, $i = 1, 2$, are the transverse momenta of the two leading jets (see below for the definition). This scale has been found to reduce significantly the difference between LO and NLO QCD predictions for the VBS process at large transverse momenta [9].

Regarding the electromagnetic coupling, the G_μ scheme [46] has been used where the coupling is obtained from the Fermi constant as

$$\alpha = \frac{\sqrt{2}}{\pi} G_\mu M_W^2 \left(1 - \frac{M_W^2}{M_Z^2} \right) \quad \text{with} \quad G_\mu = 1.16637 \times 10^{-5} \text{ GeV}^{-2}. \quad (3.2)$$

The masses and widths of the massive particles read [47]

$$\begin{aligned} m_t &= 173.21 \text{ GeV}, & \Gamma_t &= 0 \text{ GeV}, \\ M_Z^{\text{OS}} &= 91.1876 \text{ GeV}, & \Gamma_Z^{\text{OS}} &= 2.4952 \text{ GeV}, \\ M_W^{\text{OS}} &= 80.385 \text{ GeV}, & \Gamma_W^{\text{OS}} &= 2.085 \text{ GeV}, \\ M_H &= 125.0 \text{ GeV}, & \Gamma_H &= 4.07 \times 10^{-3} \text{ GeV}. \end{aligned} \quad (3.3)$$

The bottom quark is considered massless and does not appear in the initial state for the process under consideration. The width of the top quark is set to zero as it is never resonant. The Higgs-boson mass is taken according to the recommendation of the Higgs cross section working group [48] with its corresponding width. The pole masses and widths entering the calculation are determined from the measured on-shell (OS) values [49] for the W and Z bosons according to

$$M_V = \frac{M_V^{\text{OS}}}{\sqrt{1 + (\Gamma_V^{\text{OS}}/M_V^{\text{OS}})^2}}, \quad \Gamma_V = \frac{\Gamma_V^{\text{OS}}}{\sqrt{1 + (\Gamma_V^{\text{OS}}/M_V^{\text{OS}})^2}}. \quad (3.4)$$

The set of acceptance cuts that we employ is inspired from Refs. [3, 5, 6] which describe searches for the VBS process at the LHC at a centre-of-mass energy of 8 TeV and 13 TeV. Experimentally, the final state of the process is required to have two equally charged leptons, missing transverse energy and at least two jets. QCD partons are clustered into jets using the anti- k_T algorithm [50] with jet-resolution parameter $R = 0.4$. Similarly, photons from real radiation are recombined with the final-state quarks into jets or with the charged leptons into dressed leptons, in both cases via the anti- k_T algorithm and a resolution parameter $R = 0.1$. Only partons with rapidity $|y| < 5$ are considered for recombination, while particles with larger $|y|$ are assumed to be lost in the beam pipe. The rapidity y and the transverse momentum p_T of a particle are defined as

$$y = \frac{1}{2} \ln \frac{E + p_z}{E - p_z}, \quad p_T = \sqrt{p_x^2 + p_y^2}, \quad (3.5)$$

where E is the energy of the particle, p_z the component of its momentum along the beam axis, and p_x, p_y the components perpendicular to the beam axis.

The charged leptons ℓ are required to fulfil the acceptance cuts

$$p_{T,\ell} > 20 \text{ GeV}, \quad |y_\ell| < 2.5, \quad \Delta R_{\ell\ell} > 0.3. \quad (3.6)$$

The distance ΔR_{ij} between two particles i and j in the rapidity–azimuthal-angle plane reads

$$\Delta R_{ij} = \sqrt{(\Delta\phi_{ij})^2 + (\Delta y_{ij})^2}, \quad (3.7)$$

with $\Delta\phi_{ij} = \min(|\phi_i - \phi_j|, 2\pi - |\phi_i - \phi_j|)$ being the azimuthal-angle difference and $\Delta y_{ij} = y_i - y_j$ the rapidity difference. The missing transverse energy is required to fulfil

$$E_{T,\text{miss}} = p_{T,\text{miss}} > 40 \text{ GeV} \quad (3.8)$$

and is computed as the transverse momentum of the sum of the two neutrino momenta. A QCD parton system after recombination is called a jet if it obeys the jet-identification criteria

$$p_{T,j} > 30 \text{ GeV}, \quad |y_j| < 4.5, \quad \Delta R_{j\ell} > 0.3, \quad (3.9)$$

where the last condition requires a minimal distance between a jet and each of the charged leptons. The identified jets are then ordered according to the size of their transverse momenta. On the invariant mass and rapidity separation of the leading and sub-leading jets, *i.e.* on the two jets with largest transverse momenta, the following VBS cuts are applied:

$$m_{jj} > 500 \text{ GeV}, \quad |\Delta y_{jj}| > 2.5. \quad (3.10)$$

Note that the two leading jets are used in the definition of the dynamical scale in Eq. (3.1) and are also referred to as tagging jets.

3.2 Integrated cross section

We start by reporting the fiducial cross section at leading order in Table 2. The scale dependence of the results has been studied upon varying the factorisation and renormalisation scales independently. Specifically, the central scale defined in Eq. (3.1) has been scaled by factors ξ_{fac} and ξ_{ren} for the combinations

$$(\xi_{\text{fac}}, \xi_{\text{ren}}) \in \{ (1/2, 1/2), (1/2, 1), (1, 1/2), (1, 1), (1, 2), (2, 1), (2, 2) \}, \quad (3.11)$$

where $(\xi_{\text{fac}}, \xi_{\text{ren}}) = (1, 1)$ corresponds to the central scale. For each cross section, three values are given: the one corresponding to the central scale, the maximum, and the minimum. For the fiducial cross section, the sum of the contributions of all orders is computed for each scale choice separately, and then the maximum and the minimum are extracted. The order $\mathcal{O}(\alpha^6)$ corresponds to the EW-induced contribution, the order $\mathcal{O}(\alpha_s^2\alpha^4)$ to the QCD-induced contribution, and the order $\mathcal{O}(\alpha_s\alpha^5)$ represents the interferences. For the fiducial volume with

Order	$\mathcal{O}(\alpha^6)$	$\mathcal{O}(\alpha_s \alpha^5)$	$\mathcal{O}(\alpha_s^2 \alpha^4)$	Sum
σ_{LO} [fb]	1.4178(2)	0.04815(2)	0.17229(5)	1.6383(2)
$\sigma_{\text{LO}}^{\text{max}}$ [fb]	1.5443(2)	0.05680(3)	0.22821(6)	1.8293(2)
$\sigma_{\text{LO}}^{\text{min}}$ [fb]	1.3091(2)	0.04135(2)	0.13323(3)	1.4836(2)

Table 2: Fiducial cross section at LO for the process $pp \rightarrow \mu^+ \nu_\mu e^+ \nu_e jj$, stated separately for the orders $\mathcal{O}(\alpha^6)$, $\mathcal{O}(\alpha_s \alpha^5)$, and $\mathcal{O}(\alpha_s^2 \alpha^4)$ and for the sum of all the LO contributions expressed in femtobarn. The cross section σ_{LO} corresponds to the central scale choice, while the cross sections $\sigma_{\text{LO}}^{\text{max}}$ and $\sigma_{\text{LO}}^{\text{min}}$ correspond to the scale choices leading to the maximum and minimum cross section, respectively. The statistical uncertainty from the Monte Carlo integration on the last digit is given in parenthesis.

VBS cuts defined in the previous section, the EW-induced process is clearly dominating over its irreducible background processes. It amounts to 87% of the cross section of the full process $pp \rightarrow \mu^+ \nu_\mu e^+ \nu_e jj$, while the $\mathcal{O}(\alpha_s^2 \alpha^4)$ contributions add up to about 10%. The impact of the interferences on the fiducial cross section is small, at the level of 3%. The contribution of individual channels is actually larger since interferences enter with positive and negative sign (*e.g.* +4% for the uu channel and -1.2% for the $u\bar{d}$ channels) and not all channels involve interferences. The smallness of the interferences is not unexpected, since by construction, resonances in interfered t - u -channel or s - t / u -channel diagrams are suppressed with respect to kinematic topologies from squared resonant s -, t - or u -channel diagrams present in the order $\mathcal{O}(\alpha^6)$ and $\mathcal{O}(\alpha_s^2 \alpha^4)$ contributions. At leading order, we find a scale dependence of $[+8.9\%; -7.7\%]$, $[+17.9\%; -14.1\%]$, $[+32.5\%; -22.7\%]$ for the contributions of orders $\mathcal{O}(\alpha^6)$, $\mathcal{O}(\alpha_s \alpha^5)$, $\mathcal{O}(\alpha_s^2 \alpha^4)$, respectively, leading to

$$\sigma_{\text{LO}} = 1.6383(2)_{-9.44(2)\%}^{+11.66(2)\%} \text{ fb.} \quad (3.12)$$

Naturally the scale dependence is larger for contributions depending on the strong coupling.

In Table 3, all NLO corrections to the fiducial cross sections split into contributions of the different orders in the strong and EW coupling are presented. In the following, the relative NLO corrections are always normalised to the sum of all LO contributions. The total correction to the full process is large and negative, amounting to -17.1% . The bulk of the correction with -13.2% stems from the order $\mathcal{O}(\alpha^7)$, the EW correction to the EW-induced process. Note that the correction is smaller than the -16.0% stated in Ref. [15], mainly owing to the normalisation to the sum of all LO contributions instead of to the $\mathcal{O}(\alpha^6)$ contribution alone. The remaining additional difference due to the dynamical scale choice is small ($+0.7\%$) as this affects the purely EW contribution only via the evolution of the PDF and not via the running in α_s . The second-largest corrections with -3.5% occur at order $\mathcal{O}(\alpha_s \alpha^6)$. The contribution of order $\mathcal{O}(\alpha_s^3 \alpha^4)$ with a correction of -0.4% is suppressed by another order of magnitude. The contribution of order $\mathcal{O}(\alpha_s^2 \alpha^5)$ is even more suppressed and phenomenologically unimportant

Order	$\mathcal{O}(\alpha^7)$	$\mathcal{O}(\alpha_s \alpha^6)$	$\mathcal{O}(\alpha_s^2 \alpha^5)$	$\mathcal{O}(\alpha_s^3 \alpha^4)$	Sum
$\delta\sigma_{\text{NLO}}$ [fb]	-0.2169(3)	-0.0568(5)	-0.00032(13)	-0.0063(4)	-0.2804(7)
$\delta\sigma_{\text{NLO}}/\sigma_{\text{LO}}$ [%]	-13.2	-3.5	0.0	-0.4	-17.1

Table 3: NLO corrections for the process $pp \rightarrow \mu^+ \nu_\mu e^+ \nu_e jj$ at the orders $\mathcal{O}(\alpha^7)$, $\mathcal{O}(\alpha_s \alpha^6)$, $\mathcal{O}(\alpha_s^2 \alpha^5)$, and $\mathcal{O}(\alpha_s^3 \alpha^4)$ and for the sum of all NLO corrections. The contribution $\delta\sigma_{\text{NLO}}$ corresponds to the absolute correction for the central scale choice while $\delta\sigma_{\text{NLO}}/\sigma_{\text{LO}}$ gives the relative correction normalised to the sum of all LO contributions at the central scale. The absolute contributions are expressed in femtobarn while the relative ones are expressed in per cent. The statistical uncertainty from the Monte Carlo integration on the last digit is given in parenthesis.

at the fiducial cross-section level. The hierarchy of the NLO corrections follows roughly the pattern observed at LO: at the integrated cross-section level, each NLO correction is roughly one order of magnitude smaller than the corresponding LO contribution. Thus, one expects that the bulk of the $\mathcal{O}(\alpha_s \alpha^6)$ corrections stems from the QCD corrections to the EW-induced process, while only a small contribution results from the EW corrections to the interference. We emphasise, however, again that QCD corrections to the EW-induced process and EW corrections to the LO interference cannot be defined independently. Indeed, using the full matrix element, they both contribute at the order $\mathcal{O}(\alpha_s \alpha^6)$ as discussed in Sect. 2.2. The contributions at the order $\mathcal{O}(\alpha_s^2 \alpha^5)$ are small because the corresponding LO contributions are already suppressed and moreover the EW corrections to the QCD-induced LO contribution and the QCD corrections to the LO interference cancel to a large extent. Upon calculating the NLO cross section with the different scales of Eq. (3.11), we find

$$\sigma_{\text{NLO}} = 1.3577(7)^{+1.2(1)\%}_{-2.7(1)\%} \text{ fb}, \quad (3.13)$$

i.e. a reduction of the LO scale dependence by a factor five.

We have also calculated the photon-induced NLO contributions as shown in Table 4. Since the photon PDF from the NNPDF-3.0 QED set is known to give rather sizeable contributions with a large error, we have also calculated these contributions using the PDF of the recent LUXqed_plus_PDF4LHC15_nnlo_100 set [51]. For LUXqed we use the $\overline{\text{MS}}$ factorisation scheme throughout, while we have verified that the effect of the factorisation scheme is irrelevant at the level of accuracy of the results given. The photon-induced NLO contributions are dominated by those of order $\mathcal{O}(\alpha^7)$ and amount to 2.7% based on NNPDF-3.0 QED and 1.5% based on LUXqed. The photon-induced contributions of orders $\mathcal{O}(\alpha_s \alpha^6)$ and $\mathcal{O}(\alpha_s^2 \alpha^5)$ are negligible. Hence in the following, only the photon-induced contributions of order $\mathcal{O}(\alpha^7)$ are displayed in the distributions. Note that in our definition of the NLO corrections at order $\mathcal{O}(\alpha^7)$, the photon-induced contributions are not included but are shown separately. This means that for the combined distributions (Fig. 7), the NLO predictions do not include the photon-induced contributions.

Order	PDF	$\mathcal{O}(\alpha^7)$	$\mathcal{O}(\alpha_s \alpha^6)$	$\mathcal{O}(\alpha_s^2 \alpha^5)$
$\delta\sigma_{\text{NLO}}$ [fb]	NNPDF-3.0 QED	0.04368(2)	$< 10^{-6}$	0.000074(1)
$\delta\sigma_{\text{NLO}}/\sigma_{\text{LO}}$ [%]	NNPDF-3.0 QED	+2.66	< 0.0001	+0.004
$\delta\sigma_{\text{NLO}}/\sigma_{\text{LO}}$ [%]	LUXqed	+1.51	< 0.0001	+0.002

Table 4: Photon-induced NLO corrections for the process $pp \rightarrow \mu^+ \nu_\mu e^+ \nu_e jj$ at the orders $\mathcal{O}(\alpha^7)$, $\mathcal{O}(\alpha_s \alpha^6)$, and $\mathcal{O}(\alpha_s^2 \alpha^5)$ in both absolute (expressed in femtobarn) and relative value (expressed in per cent) for the PDF set NNPDF-3.0 QED. In addition, the relative corrections are also given for the LUXqed PDF set.

Set-up of Ref. [7]	Present work	DHK [9]	JOZ [7]
σ_{LO} [fb]	1.4038(4)	1.4061(7)	1.409
σ_{NLO} [fb]	1.380(1)	1.372(1)	1.372

Table 5: Comparison of fiducial cross sections at LO [order $\mathcal{O}(\alpha^6)$] and NLO [order $\mathcal{O}(\alpha_s \alpha^6)$] for the process $pp \rightarrow \mu^+ \nu_\mu e^+ \nu_e jj$ against the literature in the set-up of Ref. [7] with MSTW08 PDF. DHK denotes the calculation of Ref. [9], while JOZ refers to the one of Ref. [7]. The cross sections are expressed in femtobarn and the statistical uncertainty from the Monte Carlo integration on the last digit is given in parenthesis.

So far, all computations in the literature at the order $\mathcal{O}(\alpha_s \alpha^6)$ [7–9] have been done in the so-called VBS approximation. This features the inclusion of t - and u -channel diagrams but neglects their interferences as well as s -channel contributions. In order to assess the quality of this approximation, we have re-computed the full $\mathcal{O}(\alpha_s \alpha^6)$ corrections without VBS approximation in the set-ups of Refs. [7] and [9]. In Table 5, a comparison of LO and NLO fiducial cross sections is presented in the set-up of Ref. [7]. In Table 6, results are compared with those of Ref. [9]². At the level of the fiducial cross section, the approximate calculations turn out to agree within 0.6% with the full computation presented here at both LO [order $\mathcal{O}(\alpha^6)$] and NLO [order $\mathcal{O}(\alpha_s \alpha^6)$]. In addition, a modified version of RECOLA allowed us to confirm a difference of 0.6% at NLO between the full computation and the VBS approximation in our set-up.

3.3 Differential distributions

We start the discussion of differential distributions with plots showing all the different contributions in the strong and EW coupling at both LO and NLO. In the upper panel, the three LO contributions as well as the full NLO prediction are plotted. In the two lower panels, the four contributions to the relative NLO corrections normalised to the sum of all the LO contri-

²Note that the LO cross section reported here for Ref. [9] corresponds to the approximate calculation.

Set-up of Ref. [9]	Present work	DHK [9]
σ_{LO} [fb]	1.2230(4)	1.2218(2)
σ_{NLO} [fb]	1.2975(15)	1.2917(8)

Table 6: Comparison of fiducial cross sections at LO [order $\mathcal{O}(\alpha^6)$] and NLO [order $\mathcal{O}(\alpha_s\alpha^4)$] for the process $pp \rightarrow \mu^+\nu_\mu e^+\nu_e jj$ against the literature in the set-up of Ref. [9]. DHK denotes the results of Ref. [9]. The cross sections are expressed in femtobarn and the statistical uncertainty from the Monte Carlo integration on the last digit is given in parenthesis.

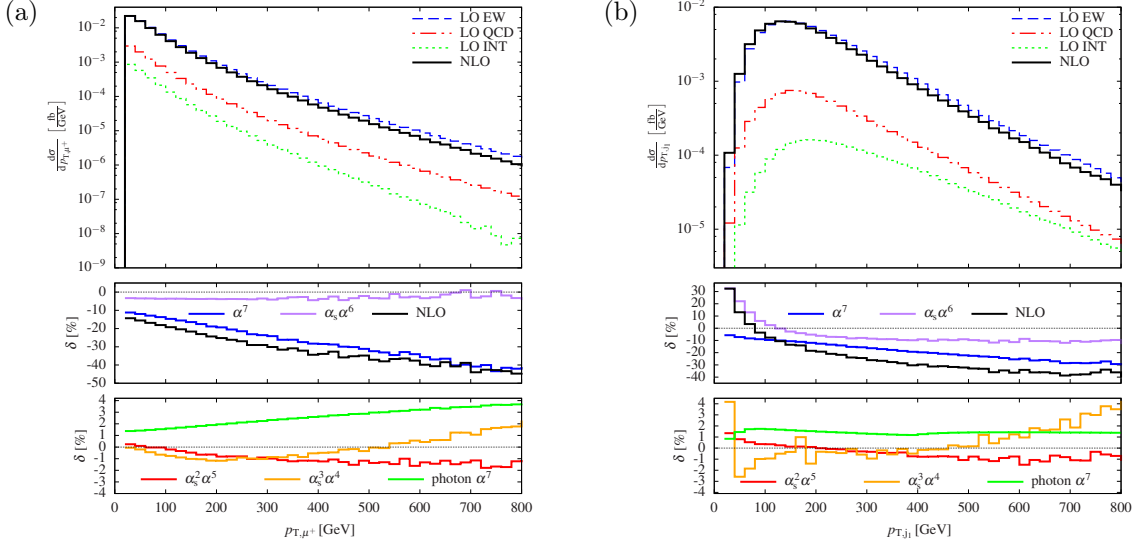


Figure 5: Transverse-momentum distributions at a centre-of-mass energy $\sqrt{s} = 13$ TeV at the LHC for $pp \rightarrow \mu^+\nu_\mu e^+\nu_e jj$: (a) for the anti-muon (left) and (b) the hardest jet (right). The upper panels show the three LO contributions as well as the sum of all NLO predictions. The two lower panels show the relative NLO corrections with respect to the full LO, defined as $\delta_i = \delta\sigma_i / \sum \sigma_{\text{LO}}$, where $i = \mathcal{O}(\alpha^7), \mathcal{O}(\alpha_s\alpha^6), \mathcal{O}(\alpha_s^2\alpha^5), \mathcal{O}(\alpha_s^3\alpha^4)$. In addition, the NLO photon-induced contributions of order $\mathcal{O}(\alpha^7)$ computed with LUXqed is provided separately.

butions are presented along with the NLO photon-induced contributions of order $\mathcal{O}(\alpha^7)$. The latter are computed for the LUXqed PDF and are thus normalised to the Born contributions obtained with the corresponding PDF. Remember that these photon-induced contributions are not included in our definition of the NLO corrections of order $\mathcal{O}(\alpha^7)$.

In Fig. 5, two transverse-momentum distributions are displayed. Starting with the distribution in the transverse momentum of the anti-muon, the upper panel in Fig. 5a shows that the EW-induced contribution is dominant over the whole phase space. Concerning the relative NLO corrections in the lower panel, the largest contribution is the one of order $\mathcal{O}(\alpha^7)$. It ranges from -10% at 20 GeV (the cut on the transverse momentum of the charged lepton) to -40% at 800 GeV. The large corrections for high transverse momenta are due to logarithms of

EW origin, the so-called Sudakov logarithms, as already pointed out in Ref. [15]. The second largest contribution is the one of order $\mathcal{O}(\alpha_s \alpha^6)$ which consists of QCD corrections to the EW-induced contribution and EW corrections to the interference. Over the considered range, this contribution stays between -4% and 0% . While the corrections of order $\mathcal{O}(\alpha_s^2 \alpha^5)$ are negligible at the level of the fiducial cross section, they reach -2% for $p_{T,\mu^-} = 800$ GeV. The corrections of orders $\mathcal{O}(\alpha_s^3 \alpha^4)$ stay also below 2% in magnitude and cancel those of order $\mathcal{O}(\alpha_s^2 \alpha^5)$ for large p_{T,μ^-} . While the $\mathcal{O}(\alpha_s^2 \alpha^5)$ contributions decrease owing to the presence of Sudakov logarithms, the $\mathcal{O}(\alpha_s^3 \alpha^4)$ contributions steadily increase above $p_{T,\mu^+} = 200$ GeV. The photon-induced contributions increase from 1.5% to 4% with increasing p_{T,μ^+} , while for other distributions they are smaller and mostly do not show any shape distortion. This is in accordance with what has been found for LO photon-induced contributions for $pp \rightarrow e^+ \nu_e \mu^- \bar{\nu}_\mu b \bar{b} H$ [29].

Figure 5b shows the distribution in the transverse momentum of the leading jet. While there was a clear hierarchy between the LO contributions in the previous observable, here the LO interference becomes comparable to the QCD-induced process around 800 GeV (see also Ref. [13]). Strikingly, the shape of the distribution at low transverse momentum is rather different. By construction, for small transverse momentum of the leading jet, the transverse momenta of all sub-leading jets must be small as well. This suppresses the available phase space and explains why the LO distribution is less peaked at small transverse momenta as compared to the distributions in the transverse momentum of the anti-muon (Fig. 5a) or the transverse momentum of the sub-leading jet (not shown). Concerning the NLO contributions, the main difference with respect to the distribution in the transverse momentum of the muon is the behaviour of the $\mathcal{O}(\alpha_s \alpha^6)$ corrections: they are large and positive at the kinematical threshold of 30 GeV (at the level of 30%), decrease towards -5% around 200 GeV and stay almost constant over the whole spectrum up to 800 GeV. The large QCD corrections for small p_{T,j_1} have already been observed in Ref. [9] for the same dynamical scale. The strong increase of the QCD corrections at low p_T , which is also present in the results of Ref. [13], is a kinematical effect genuine to the distribution in the transverse momentum of the leading jet and is independent of the QCD scale. As observed also in Refs. [52, 53] at NLO and NNLO QCD for Higgs-boson production in vector-boson fusion, the QCD corrections have the effect of redistributing jets from higher to lower transverse momenta. This behaviour is mainly driven by the real radiation and causes a large effect for small p_{T,j_1} where the LO contribution is suppressed. The contributions of orders $\mathcal{O}(\alpha_s^2 \alpha^5)$ and $\mathcal{O}(\alpha_s^3 \alpha^4)$ behave qualitatively similar as for the p_{T,μ^+} distribution.

The distributions in the rapidities of the anti-muon and of the hardest jet are displayed in Figs. 6a and 6b, respectively. As Fig. 6a shows, the anti-muons are mostly produced in the central region of the detector for the EW-induced process, while for the QCD-induced contribution, although suppressed, they lie preferentially at rapidities around ± 2 . The interference, even more suppressed, is largest in the central region. The relative NLO contributions also display different behaviours. The contributions of order $\mathcal{O}(\alpha^7)$ and $\mathcal{O}(\alpha_s \alpha^6)$ are maximally negative in the central region and decrease in magnitude in the peripheral region. On the

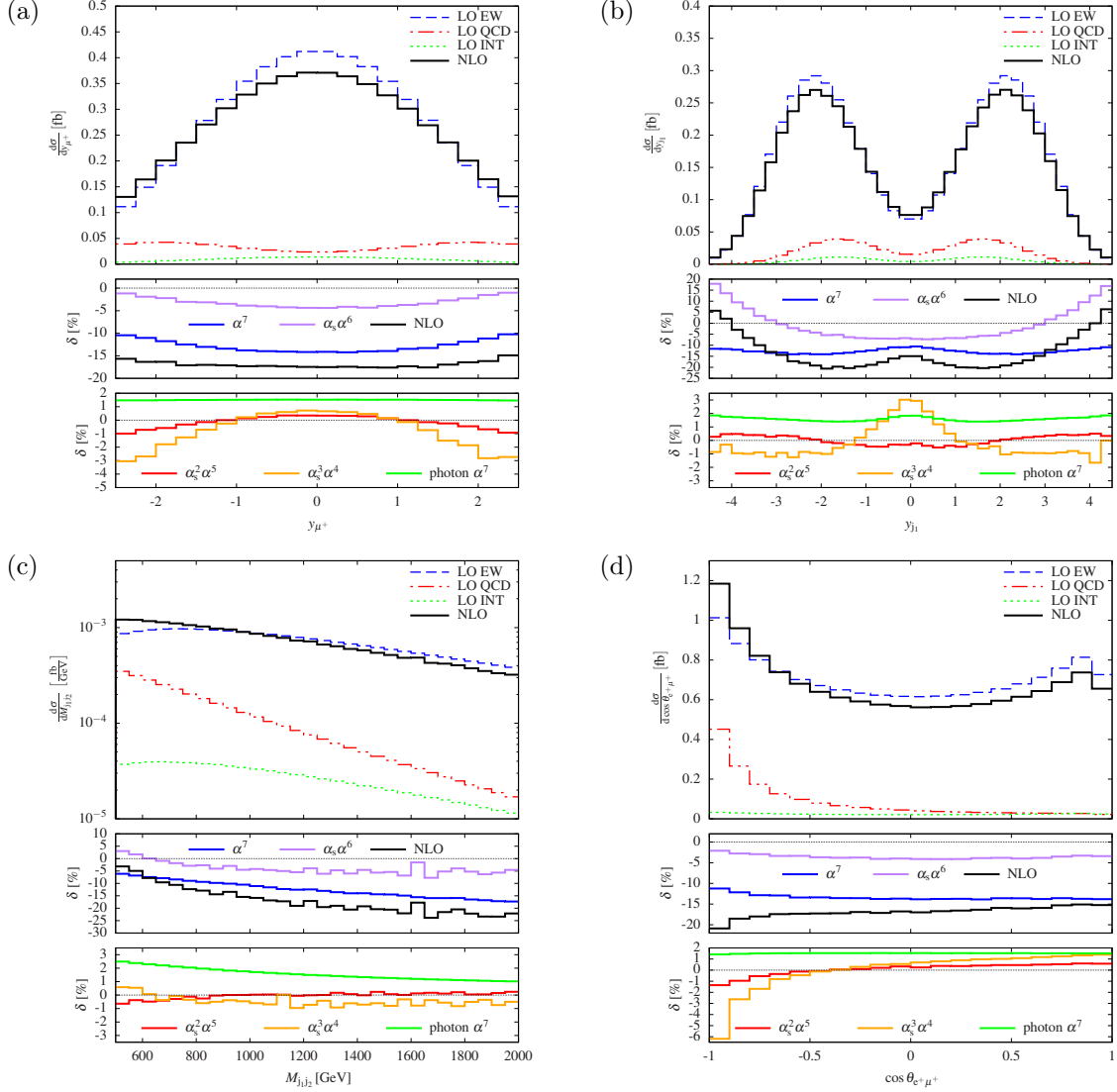


Figure 6: Differential distributions at a centre-of-mass energy $\sqrt{s} = 13$ TeV at the LHC for $pp \rightarrow \mu^+ \nu_\mu e^+ \nu_e jj$: (a) rapidity for the anti-muon (top left), (b) rapidity for the hardest jet (top right), (c) invariant mass for the two leading jets (bottom left), and (d) cosine of the angle between the positron and the anti-muon (bottom right). The upper panels show the three LO contributions as well as the sum of all NLO predictions. The two lower panels show the relative NLO corrections with respect to the full LO in per cent, defined as $\delta_i = \delta\sigma_i / \sum \sigma_{\text{LO}}$, where $i = \mathcal{O}(\alpha^7), \mathcal{O}(\alpha_s \alpha^6), \mathcal{O}(\alpha_s^2 \alpha^5), \mathcal{O}(\alpha_s^3 \alpha^4)$. In addition, the NLO photon-induced contributions of order $\mathcal{O}(\alpha^7)$ computed with LUXqed is provided separately.

other hand, the contributions of order $\mathcal{O}(\alpha_s^2 \alpha^5)$ and $\mathcal{O}(\alpha_s^3 \alpha^4)$ display an opposite behaviour with a small positive maximum in the central region and larger negative corrections in the forward and backward directions, which is mainly caused by the increased relative size of

the QCD-induced LO contributions. Like for the fiducial cross section, the hierarchy of the corrections follows closely the LO contributions which is expected as the anti-muon rapidity distribution is rather flat.

The rapidity of the hardest jet (Fig. 6b) also displays interesting patterns. In the absolute prediction, one sees the typical VBS kinematic with central rapidity gap. The EW corrections to the EW-induced contribution of order $\mathcal{O}(\alpha^7)$ are larger in the region where the VBS process is dominating while they are smaller in the central region, which is typically dominated by non-VBS configurations. This observable has already been discussed in Ref. [15]. The corrections of order $\mathcal{O}(\alpha_s \alpha^6)$ are negative in the central region at a level of -5% , but around $+18\%$ for rapidity of ± 4.5 . Such a behaviour of the QCD corrections was also found in Ref. [9] for the considered process and for Higgs production via vector-boson fusion in Ref. [54]. Hence the QCD corrections have the effect of making the leading jet more forward. The corrections of order $\mathcal{O}(\alpha_s^2 \alpha^5)$ are flat and below 1% in magnitude. Those of order $\mathcal{O}(\alpha_s^3 \alpha^4)$ reach $+3\%$ in the central region but are at the level of -1% for large rapidities.

In Fig. 6c, the distribution in the invariant mass of the two tagging jets is displayed. As pointed out already in Ref. [15], at LO the VBS contribution extends to large invariant masses. The QCD-induced one drops significantly faster to become an order of magnitude smaller than the VBS contribution at 1200 GeV . This illustrates the need for VBS-specific event selections. Indeed, by extrapolating to lower invariant mass, it is clear that in this region the QCD-induced process would be sizeable. As for the EW-induced process, the interference contribution displays a comparably flat behaviour becoming of the same size as the QCD-induced one around 2000 GeV . The relative NLO corrections are similar to those for the distributions in the transverse momenta. The EW corrections to the EW-induced process display the typical behaviour of Sudakov logarithms in the high-invariant-mass region and grow negatively large towards high invariant masses. The contributions of order $\mathcal{O}(\alpha_s \alpha^6)$ are positive for $M_{j_1 j_2} = 500 \text{ GeV}$ but tend to -5% at high invariant masses. The contributions of order $\mathcal{O}(\alpha_s^2 \alpha^5)$ and $\mathcal{O}(\alpha_s^3 \alpha^4)$ are below 1% in magnitude and tend to compensate each other. The photon-induced contributions slightly exceed 2% for small invariant mass and decrease for higher invariant masses.

Finally, we consider the distribution in the cosine of the angle between the positron and the anti-muon in Fig. 6d. The absolute prediction nicely illustrates that the charged leptons produced via the QCD-induced mechanism are mainly back to back while the EW-induced process has a maximum both for the back-to-back and the collinear configurations (the drop in the last bin is due to the cut on $\Delta R_{\ell\ell}$). The latter arise from configurations with a strongly boosted VBS system that does not occur in QCD-induced topologies. The observable is thus an example of a relatively inclusive quantity where the ratio of the VBS and QCD-induced contributions vary in shape in phase space. While the QCD-induced contributions are strongly suppressed for small and intermediate angles, they are of the same order of magnitude as the EW contributions for very large angles. The interference contribution is relatively constant over the whole spectrum and strongly suppressed. The $\mathcal{O}(\alpha^7)$ and $\mathcal{O}(\alpha_s \alpha^6)$ corrections both vary steadily with increasing $\cos \theta_{e+\mu^-}$ from -11% to -14% and from -3% to

−4%, respectively. The corrections are of the same order as for the fiducial cross section. The $\mathcal{O}(\alpha_s^3\alpha^4)$ contribution is small for small angles but increases in size to −6% for large angles, where it lies between the $\mathcal{O}(\alpha_s\alpha^6)$ and the $\mathcal{O}(\alpha^7)$ corrections. This is due to the enhanced LO QCD-induced contribution and confirms that the hierarchy of the NLO corrections is determined to a large extent by the pattern observed for the LO prediction. The contribution at order $\mathcal{O}(\alpha_s^2\alpha^5)$ has qualitatively a similar behaviour, it is however suppressed.

In Fig. 7 we present some distributions displaying the variation of the factorisation and renormalisation scales. In the upper panels, the sums of all LO contributions as well as of all NLO contributions are shown.³ The band is obtained by varying the factorisation and renormalisation scales independently by the factors ξ_{fac} and ξ_{ren} with the combinations of Eq. (3.11). The central scale is defined as $(\xi_{\text{fac}}, \xi_{\text{ren}}) = (1, 1)$. The relative corrections shown in the lower panel are normalised to the LO prediction for the central scale. In Fig. 7a, the distribution in the missing transverse momentum is displayed. The scale-uncertainty band decreases significantly by going from LO to NLO. Nonetheless, these two bands do not overlap. Indeed, as explained previously, the VBS process (which is a purely EW process) is dominating the $\mu^+\nu_\mu e^+\nu_e jj$ final state, and the NLO EW corrections to VBS represent a large fraction of the NLO corrections. These corrections have the effect of simply shifting the prediction without affecting significantly the size of the scale variation band. While missing higher-order QCD corrections can be estimated via scale variations this is not possible for higher-order EW corrections in the on-shell scheme. A conservative estimate for the higher-order EW corrections is provided by the square of the EW NLO correction, $(\delta_{\text{EW}})^2$.

In Fig. 7b, the distribution in the rapidity difference of the positron and the anti-muon is shown. As for the rapidity of the anti-muon, the bulk of the cross section is located in the central region due to the dominance of the VBS process in this region. For large rapidities, where the QCD-induced background contributions are sizeable, the LO scale variation is particularly large and the LO and NLO uncertainty bands overlap.

Finally, the distributions in the invariant masses of the positron–anti-muon system and of the two tagging jets are shown in Figs. 7c and 7d, respectively. These two observables have been considered in a recent CMS measurement [6]. The behaviour of the NLO corrections and the scale dependence is similar as for the distribution in the missing transverse momentum in Fig. 7a. Note, however, that the NLO corrections are larger for the distributions in $p_{\text{T,miss}}$ and $M_{e^+\mu^+}$ than for the one in M_{jj} . In general, the scale dependence is larger where the cross section is smaller and the NLO corrections are larger.

4 Conclusions

In this article we have presented all NLO electroweak (EW) and QCD corrections to the process $pp \rightarrow \mu^+\nu_\mu e^+\nu_e jj$ including like-sign charged vector-boson scattering (VBS) and its EW- and QCD-induced irreducible background. As the full LO and NLO matrix elements are used, these computations account for all possible off-shell, non-resonant, and interference

³The photon-induced contributions are left out of the NLO predictions.

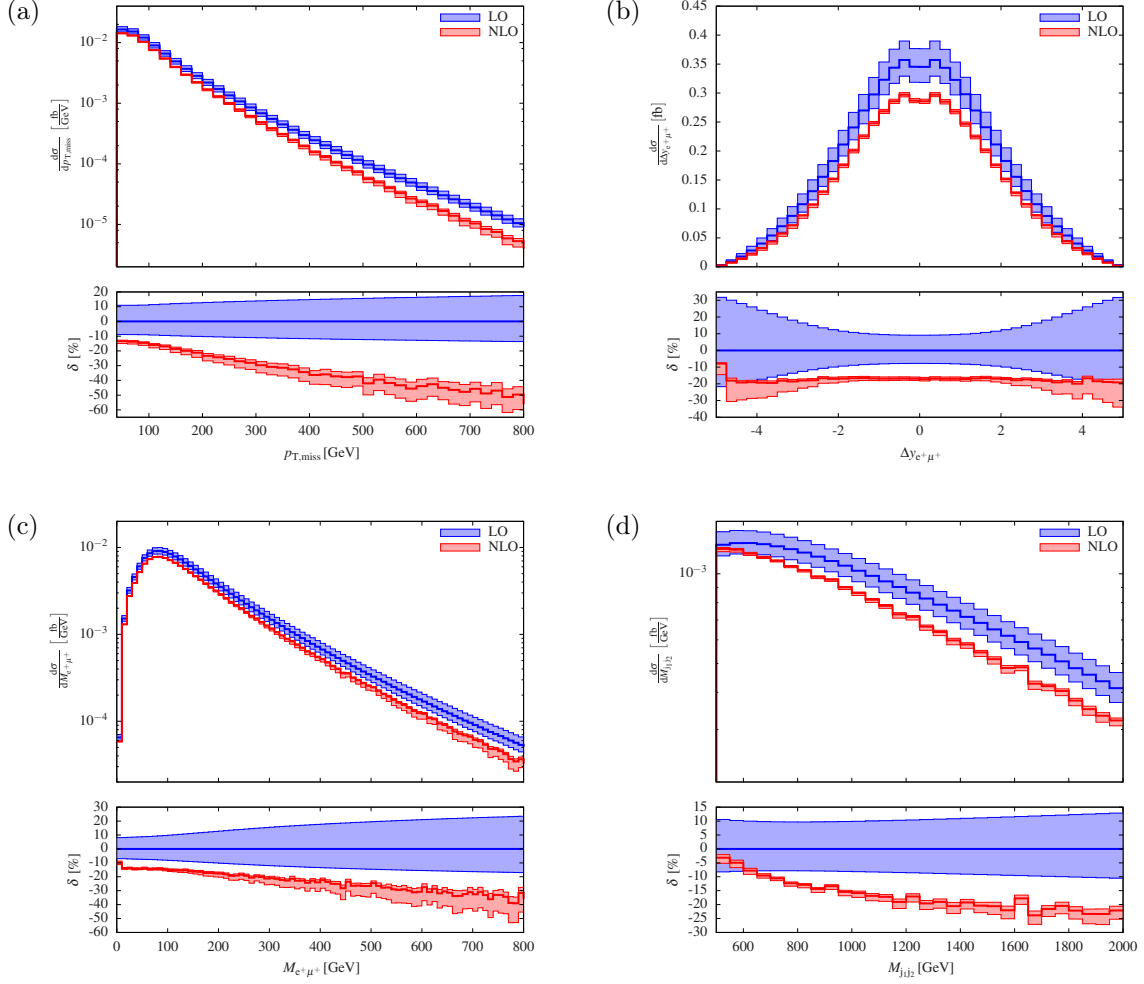


Figure 7: Differential distributions at a centre-of-mass energy $\sqrt{s} = 13$ TeV at the LHC for $pp \rightarrow \mu^+ \nu_\mu e^+ \nu_e jj$: (a) missing transverse momentum (top left), (b) rapidity separation between the positron and anti-muon (top right), (c) invariant mass of the positron and anti-muon system (bottom left), (d) invariant mass of the two tagging jets (bottom right). The upper panels show the sum of all LO and NLO contributions with scale variation. The lower panels show the relative corrections in per cent.

effects. The latter aspect plays an important role in this computation: the LO amplitude consists of a purely EW-induced part, which includes VBS, and a QCD-induced part, leading thus to three different LO contributions at the level of squared amplitudes. These are of the orders $\mathcal{O}(\alpha^6)$, $\mathcal{O}(\alpha_s \alpha^5)$, $\mathcal{O}(\alpha_s^2 \alpha^4)$ in the strong and electromagnetic couplings. At NLO, consequently, four types of corrections have been computed at the orders $\mathcal{O}(\alpha^7)$, $\mathcal{O}(\alpha_s \alpha^6)$, $\mathcal{O}(\alpha_s^2 \alpha^5)$, and $\mathcal{O}(\alpha_s^3 \alpha^4)$, respectively. For the orders $\mathcal{O}(\alpha_s \alpha^6)$ and $\mathcal{O}(\alpha_s^2 \alpha^5)$, both NLO QCD and EW corrections to different underlying Born contributions arise. These cannot be unambiguously separated as some loop diagrams contribute to both. Hence, at NLO, it is

not possible to strictly distinguish the VBS process from its irreducible QCD background processes.

We have presented predictions for the LHC running at a centre-of-mass energy of 13 TeV with realistic experimental event selections applied to the final state. In this fiducial region, results for the integrated cross-section and various distributions have been shown. In particular, predictions for the three LO contributions as well as for the four contributing NLO corrections have been presented both separately and in a combined form. This allows the experimental physicists to extract all necessary information from our calculation and to include it in their analysis.

At LO, the VBS process clearly dominates over its irreducible background processes. On the one hand, this is due to the characteristic signature of two equally charged W bosons excluding a sizeable amount of partonic channels that would mainly contribute to the QCD background. On the other hand, it is further enhanced by the specific VBS event selection. Concerning the NLO corrections, we identify the dominant contributions to be the large negative EW corrections to the VBS process. For the fiducial cross section, they reach -13% of the complete LO contributions and are even significantly more enhanced at the level of differential distributions with up to (minus) 40% corrections in the kinematical regions explored. These corrections display the typical behaviour of Sudakov logarithms that grow large in the high-energy regime. The NLO contributions of order $\mathcal{O}(\alpha_s\alpha^6)$, which are dominated by QCD corrections to the EW-induced process, are four times smaller and negative for the fiducial cross section. At the level of differential distributions, they display a different behaviour than the EW corrections. Finally, the NLO contributions of order $\mathcal{O}(\alpha_s^2\alpha^5)$ and $\mathcal{O}(\alpha_s^3\alpha^4)$ are relatively suppressed with respect to the LO prediction and even cancel partially. The dependence on the factorisation and renormalisation scale is significantly reduced upon including NLO corrections. However, this does not provide an estimate of the theoretical uncertainty from missing higher-order EW corrections. Since these are dominated by EW Sudakov logarithms, we recommend to use the squared EW corrections as a conservative estimate for this purpose.

As this article presents predictions for a realistic final state where the event selection follows the one of the experimental collaborations, this should make this computation very relevant for the measurement of the VBS process. Since at NLO it is not possible to distinguish unambiguously the VBS process from its irreducible background, we advocate for a global measurement of the $\mu^+\nu_\mu e^+\nu_e jj$ final state.

Acknowledgments

We thank Jean-Nicolas Lang and Sandro Uccirati for supporting the computer program RECOLA and Robert Feger for assistance with the Monte Carlo program MoCANLO. We acknowledge financial support by the German Federal Ministry for Education and Research (BMBF) under contract no. 05H15WWCA1 and the German Science Foundation (DFG) under reference number DE 623/6-1.

References

- [1] J. M. Campbell and R. K. Ellis, *Higgs constraints from vector boson fusion and scattering*, *JHEP* **04** (2015) 030, [[arXiv:1502.02990](#)].
- [2] D. R. Green, P. Meade, and M.-A. Pleier, *Multiboson interactions at the LHC*, *Rev. Mod. Phys.* **89** (2017) 035008, [[arXiv:1610.07572](#)].
- [3] **ATLAS** Collaboration, G. Aad et al., *Evidence for Electroweak Production of $W^\pm W^\pm jj$ in pp Collisions at $\sqrt{s} = 8$ TeV with the ATLAS Detector*, *Phys. Rev. Lett.* **113** (2014) 141803, [[arXiv:1405.6241](#)].
- [4] **ATLAS** Collaboration, M. Aaboud et al., *Measurement of $W^\pm W^\pm$ vector-boson scattering and limits on anomalous quartic gauge couplings with the ATLAS detector*, *Phys. Rev.* **D96** (2017) 012007, [[arXiv:1611.02428](#)].
- [5] **CMS** Collaboration, V. Khachatryan et al., *Study of vector boson scattering and search for new physics in events with two same-sign leptons and two jets*, *Phys. Rev. Lett.* **114** (2015) 051801, [[arXiv:1410.6315](#)].
- [6] **CMS** Collaboration, *Observation of electroweak production of same-sign W boson pairs in the two jet and two same-sign lepton final state in proton-proton collisions at 13 TeV*, 2017. CMS-PAS-SMP-17-004.
- [7] B. Jäger, C. Oleari, and D. Zeppenfeld, *Next-to-leading order QCD corrections to W^+W^+jj and W^-W^-jj production via weak-boson fusion*, *Phys. Rev.* **D80** (2009) 034022, [[arXiv:0907.0580](#)].
- [8] B. Jäger and G. Zanderighi, *NLO corrections to electroweak and QCD production of W^+W^+ plus two jets in the POWHEGBOX*, *JHEP* **11** (2011) 055, [[arXiv:1108.0864](#)].
- [9] A. Denner, L. Hošeková, and S. Kallweit, *NLO QCD corrections to W^+W^+jj production in vector-boson fusion at the LHC*, *Phys. Rev.* **D86** (2012) 114014, [[arXiv:1209.2389](#)].
- [10] M. Rauch, *Vector-Boson Fusion and Vector-Boson Scattering*, [arXiv:1610.08420](#).
- [11] T. Melia, K. Melnikov, R. Röntsch, and G. Zanderighi, *Next-to-leading order QCD predictions for W^+W^+jj production at the LHC*, *JHEP* **12** (2010) 053, [[arXiv:1007.5313](#)].
- [12] T. Melia, P. Nason, R. Röntsch, and G. Zanderighi, *W^+W^+ plus dijet production in the POWHEGBOX*, *Eur. Phys. J.* **C71** (2011) 1670, [[arXiv:1102.4846](#)].
- [13] F. Campanario, M. Kerner, L. D. Ninh, and D. Zeppenfeld, *Next-to-leading order QCD corrections to W^+W^+ and W^-W^- production in association with two jets*, *Phys. Rev.* **D89** (2014) 054009, [[arXiv:1311.6738](#)].
- [14] J. Baglio et al., *Release Note - VBFNLO 2.7.0*, [arXiv:1404.3940](#).
- [15] B. Biedermann, A. Denner, and M. Pellen, *Large electroweak corrections to vector-boson scattering at the Large Hadron Collider*, *Phys. Rev. Lett.* **118** (2017) 261801, [[arXiv:1611.02951](#)].
- [16] J. Alwall et al., *The automated computation of tree-level and next-to-leading order differential cross sections, and their matching to parton shower simulations*, *JHEP* **07** (2014) 079, [[arXiv:1405.0301](#)].

- [17] T. Melia, K. Melnikov, R. Röntsch, and G. Zanderighi, *NLO QCD corrections for W^+W^- pair production in association with two jets at hadron colliders*, *Phys. Rev.* **D83** (2011) 114043, [[arXiv:1104.2327](#)].
- [18] S. Actis et al., *Recursive generation of one-loop amplitudes in the Standard Model*, *JHEP* **04** (2013) 037, [[arXiv:1211.6316](#)].
- [19] S. Actis et al., *RECOLA: REcursive Computation of One-Loop Amplitudes*, *Comput. Phys. Commun.* **214** (2017) 140–173, [[arXiv:1605.01090](#)].
- [20] A. Denner, S. Dittmaier, and L. Hofer, *COLLIER - A fortran-library for one-loop integrals*, *PoS LL2014* (2014) 071, [[arXiv:1407.0087](#)].
- [21] A. Denner, S. Dittmaier, and L. Hofer, *COLLIER: a fortran-based Complex One-Loop Library in Extended Regularizations*, *Comput. Phys. Commun.* **212** (2017) 220–238, [[arXiv:1604.06792](#)].
- [22] A. Denner et al., *Predictions for all processes $e^+e^- \rightarrow 4 \text{ fermions} + \gamma$* , *Nucl. Phys.* **B560** (1999) 33–65, [[hep-ph/9904472](#)].
- [23] A. Denner et al., *Electroweak corrections to charged-current $e^+e^- \rightarrow 4 \text{ fermion}$ processes: Technical details and further results*, *Nucl. Phys.* **B724** (2005) 247–294, [[hep-ph/0505042](#)].
- [24] B. Biedermann, A. Denner, S. Dittmaier, L. Hofer, and B. Jäger, *Electroweak corrections to $pp \rightarrow \mu^+\mu^-e^+e^- + X$ at the LHC: a Higgs background study*, *Phys. Rev. Lett.* **116** (2016) 161803, [[arXiv:1601.07787](#)].
- [25] B. Biedermann et al., *Next-to-leading-order electroweak corrections to $pp \rightarrow W^+W^- \rightarrow 4 \text{ leptons}$ at the LHC*, *JHEP* **06** (2016) 065, [[arXiv:1605.03419](#)].
- [26] B. Biedermann, A. Denner, S. Dittmaier, L. Hofer, and B. Jäger, *Next-to-leading-order electroweak corrections to the production of four charged leptons at the LHC*, *JHEP* **01** (2017) 033, [[arXiv:1611.05338](#)].
- [27] A. Denner and R. Feger, *NLO QCD corrections to off-shell top-antitop production with leptonic decays in association with a Higgs boson at the LHC*, *JHEP* **11** (2015) 209, [[arXiv:1506.07448](#)].
- [28] A. Denner and M. Pellen, *NLO electroweak corrections to off-shell top-antitop production with leptonic decays at the LHC*, *JHEP* **08** (2016) 155, [[arXiv:1607.05571](#)].
- [29] A. Denner, J.-N. Lang, M. Pellen, and S. Uccirati, *Higgs production in association with off-shell top-antitop pairs at NLO EW and QCD at the LHC*, *JHEP* **02** (2017) 053, [[arXiv:1612.07138](#)].
- [30] S. Catani and M. H. Seymour, *A general algorithm for calculating jet cross-sections in NLO QCD*, *Nucl. Phys.* **B485** (1997) 291–419, [[hep-ph/9605323](#)]. [Erratum: *Nucl. Phys.* **B510** (1998) 503].
- [31] S. Dittmaier, *A general approach to photon radiation off fermions*, *Nucl. Phys.* **B565** (2000) 69–122, [[hep-ph/9904440](#)].
- [32] G. 't Hooft and M. J. G. Veltman, *Scalar one-loop integrals*, *Nucl. Phys.* **B153** (1979) 365–401.
- [33] W. Beenakker and A. Denner, *Infrared divergent scalar box integrals with applications in the electroweak standard model*, *Nucl. Phys.* **B338** (1990) 349–370.
- [34] S. Dittmaier, *Separation of soft and collinear singularities from one loop N point integrals*, *Nucl. Phys.* **B675** (2003) 447–466, [[hep-ph/0308246](#)].

- [35] A. Denner and S. Dittmaier, *Scalar one-loop 4-point integrals*, *Nucl. Phys.* **B844** (2011) 199–242, [[arXiv:1005.2076](#)].
- [36] G. Passarino and M. J. G. Veltman, *One-loop corrections for e^+e^- annihilation into $\mu^+\mu^-$ in the Weinberg model*, *Nucl. Phys.* **B160** (1979) 151–207.
- [37] A. Denner and S. Dittmaier, *Reduction of one-loop tensor 5-point integrals*, *Nucl. Phys.* **B658** (2003) 175–202, [[hep-ph/0212259](#)].
- [38] A. Denner and S. Dittmaier, *Reduction schemes for one-loop tensor integrals*, *Nucl. Phys.* **B734** (2006) 62–115, [[hep-ph/0509141](#)].
- [39] V. Hirschi, et al., *Automation of one-loop QCD corrections*, *JHEP* **05** (2011) 044, [[arXiv:1103.0621](#)].
- [40] **NNPDF** Collaboration, R. D. Ball et al., *Parton distributions with QED corrections*, *Nucl. Phys.* **B877** (2013) 290–320, [[arXiv:1308.0598](#)].
- [41] **NNPDF** Collaboration, R. D. Ball et al., *Parton distributions for the LHC Run II*, *JHEP* **04** (2015) 040, [[arXiv:1410.8849](#)].
- [42] J. R. Andersen et al., *Les Houches 2013: Physics at TeV Colliders: Standard Model Working Group Report*, [[arXiv:1405.1067](#)].
- [43] A. Buckley, et al., *LHAPDF6: parton density access in the LHC precision era*, *Eur. Phys. J.* **C75** (2015) 132, [[arXiv:1412.7420](#)].
- [44] K. P. O. Diener, S. Dittmaier, and W. Hollik, *Electroweak higher-order effects and theoretical uncertainties in deep-inelastic neutrino scattering*, *Phys. Rev.* **D72** (2005) 093002, [[hep-ph/0509084](#)].
- [45] S. Dittmaier and M. Huber, *Radiative corrections to the neutral-current Drell-Yan process in the Standard Model and its minimal supersymmetric extension*, *JHEP* **01** (2010) 060, [[arXiv:0911.2329](#)].
- [46] A. Denner, S. Dittmaier, M. Roth, and D. Wackeroth, *Electroweak radiative corrections to $e^+e^- \rightarrow WW \rightarrow 4$ fermions in double-pole approximation: The RACOONWW approach*, *Nucl. Phys.* **B587** (2000) 67–117, [[hep-ph/0006307](#)].
- [47] **Particle Data Group** Collaboration, K. A. Olive et al., *Review of Particle Physics*, *Chin. Phys.* **C38** (2014) 090001.
- [48] **LHC Higgs Cross Section Working Group** Collaboration, J. R. Andersen et al., *Handbook of LHC Higgs Cross Sections: 3. Higgs Properties*, [[arXiv:1307.1347](#)].
- [49] D. Yu. Bardin, A. Leike, T. Riemann, and M. Sachwitz, *Energy-dependent width effects in e^+e^- -annihilation near the Z-boson pole*, *Phys. Lett.* **B206** (1988) 539–542.
- [50] M. Cacciari, G. P. Salam, and G. Soyez, *The anti- k_t jet clustering algorithm*, *JHEP* **04** (2008) 063, [[arXiv:0802.1189](#)].
- [51] A. Manohar, P. Nason, G. P. Salam, and G. Zanderighi, *How bright is the proton? A precise determination of the photon parton distribution function*, *Phys. Rev. Lett.* **117** (2016) 242002, [[arXiv:1607.04266](#)].

- [52] M. Cacciari, F. A. Dreyer, A. Karlberg, G. P. Salam, and G. Zanderighi, *Fully differential Vector-Boson-Fusion Higgs production at Next-to-Next-to-Leading Order*, *Phys. Rev. Lett.* **115** (2015) 082002, [[arXiv:1506.02660](#)].
- [53] M. Rauch and D. Zeppenfeld, *Jet clustering dependence of Higgs boson production in vector-boson fusion*, *Phys. Rev.* **D95** (2017) 114015, [[arXiv:1703.05676](#)].
- [54] T. Figy, C. Oleari, and D. Zeppenfeld, *Next-to-leading order jet distributions for Higgs boson production via weak boson fusion*, *Phys. Rev.* **D68** (2003) 073005, [[hep-ph/0306109](#)].